

Near-threshold aeolian sand transport: Effects of boundary layer flow conditions

Ting Jin¹, Lifeng Zhou²

¹ School of Metallurgical and Energy Engineering, Kunming University of Science and Technology, Kunming, 650000, China

² Yunnan Key Laboratory of Efficient Utilization and Intelligent Control of Agricultural Water Resources, Kunming University of Science and Technology, Kunming, 650000, China

Corresponding to: Lifeng Zhou (zhoulf@kust.edu.cn)

Abstract

Boundary layer thickness is a critical factor in aeolian sand transport, as it governs the scale of energy-containing turbulent structures, yet its specific mechanisms remain inadequately quantified. Previous studies have established the role of turbulence in particle entrainment but often overlook systematic variations in boundary layer thickness. This study aims to clarify how boundary layer thickness modulates wall-shear stress fluctuations, threshold wind velocities, sand flux, and particle kinematics. We use the three-dimensional large-eddy simulation coupled with a saltation model to investigate these interactions. Results reveal that increased boundary layer thickness enhances extreme-value probability density of wall-shear stress and significantly lowers impact entrainment and rebound thresholds—the latter dropping to less than 50% of conventional wind-tunnel values. Sand transport response is velocity-dependent: at low velocities, transport rises markedly with thickness under fluid-driven entrainment; the effect diminishes at moderate velocities; and at high velocities, transport scales proportionally with thickness under splash-dominated entrainment. Moreover, thicker boundary layers intensify near-bed particle activity, elevating particle velocities and concentrations, reducing variability, increasing saltation height, and enlarging mean and variance of airborne particle diameters. These findings elucidate how boundary layer thickness modulates aeolian sand transport via turbulence–particle interactions, offering key insights for improving atmospheric and climate models and advancing the physics of turbulence-driven sediment transport in atmospheric boundary layer.

Keywords: Boundary layer thickness; Aeolian sand transport; Turbulent structures; Threshold wind velocity; Atmospheric boundary layer

33 1. Introduction

34 Wind-driven soil particle movement, also known as aeolian transport, is a key geological and
35 climatic process in arid and desert regions (Shao, 2008). Near-threshold aeolian sand transport
36 occurs around the threshold wind velocity and is characterized by intermittent bursts of intense
37 activity separated by quiescent periods (Stout and Zobeck, 1997; Leenders et al., 2005; Carneiro et
38 al., 2015; Martin and Kok, 2018). Driven by natural wind, this highly unstable process significantly
39 contributes to total mass flux and plays a crucial role in dune evolution, soil erosion, and dust
40 emission. However, its quantitative prediction remains challenging (Martin and Kok, 2018) due to
41 the multiscale nature of turbulent wind fluctuations (Butterfield, 1998; Mathis et al., 2009; Huang
42 et al., 2020; Zhang et al., 2022) and the path-dependent response of sediment transport to these
43 fluctuations (Kok, 2010a).

44 Accurate prediction of transport rate and intensity is essential for understanding the formation
45 and evolution of aeolian landforms (Sherman et al., 1998). Modeling efforts have combined
46 theoretical, experimental, and numerical approaches. Early theoretical models, such as Kawamura
47 (1951), incorporated a critical shear velocity for initial aerodynamic entrainment of particles from
48 a static bed by fluid forces alone (the fluid threshold, $u_*^t = A[gd_p(\rho_p - \rho) / \rho]^{1/2}$, where d_p is
49 particle diameter, ρ_p and ρ are particle and air densities, respectively), and proposed a cubic
50 relationship between transport rate and friction velocity above this threshold, following Bagnold
51 (1941) formulation (coefficient $A = 0.1$). Kok (2010b) later extended White's (1979) model by
52 introducing a probabilistic framework. Wind tunnel experiments have been equally influential: Zhou
53 et al. (2002) tested the Bagnold ($u_* \geq 0.47 \text{ m} \cdot \text{s}^{-1}$, u_* is friction velocity) and Kawamura
54 ($u_*^t \leq u_* < 0.35 \text{ m} \cdot \text{s}^{-1}$) equations under different wind velocities and highlighted the central role of
55 threshold velocity. Dong et al. (2003) showed that the threshold coefficient (A) decreases linearly
56 with particle Reynolds number. Creyssels et al. (2009) observed a quadratic, rather than cubic,
57 dependence of transport on friction velocity near the threshold, consistent with numerical
58 simulations by Almeida et al. (2006) using Reynolds-averaged methods (critical shear velocity =
59 $0.35 \text{ m} \cdot \text{s}^{-1}$).

60 Despite these advances, most models assume steady, continuous sediment transport governed
61 by a single fluid threshold. They fail to capture near-threshold behavior where other critical
62 velocities, such as the impact entrainment threshold (for sustaining continuous transport) and the
63 rebound threshold (for compensating energy loss from particle bouncing), are important. Predictions
64 under such conditions are therefore often inaccurate.

65 Near-threshold transport is highly intermittent and distinct from steady-state conditions
66 (Rasmussen and Sørensen, 1999). It is strongly influenced by interactions between turbulent

67 coherent structures and sand particles, with different turbulent scales acting through different
68 mechanisms (Liu et al., 2021). Boundary layer thickness is a key parameter that shapes near-wall
69 turbulence by influencing the Reynolds number, extent of the logarithmic layer, behavior of large-
70 scale structures, and distribution of turbulent energy production (Marusic et al., 2017). In wind
71 tunnels, the boundary layer thickness typically ranges from $0.1 \sim 0.2 \text{ m}$ (Clifton et al., 2006;
72 Parajuli et al., 2016; S H Li et al., 2020b), whereas in the natural atmosphere, it can reach
73 $100 \sim 200 \text{ m}$ (Wang and Zheng, 2016). Consequently, even at identical friction velocities, friction
74 Reynolds numbers may differ by orders of magnitude, leading to marked differences in transport
75 behavior.

76 Field studies have shown that sediment transport often occurs below the entrainment threshold
77 in wind tunnels (Rasmussen and Sørensen, 1999), characterized by strong spatiotemporal variability
78 (Stout and Zobeck, 1997; Baas and Sherman, 2006; Ellis et al., 2012; Huang et al., 2020).
79 Temporally, intermittent events in the field persist for much longer (Sherman et al., 2013) than in
80 wind tunnels (Wang et al., 2014). Spatially, transport commonly appears as streamers linked to
81 large-scale turbulent structures generated higher in the boundary layer (Baas and Sherman, 2005;
82 Sherman et al., 2013). Streamers in the field can be tens of times longer than those in wind tunnel
83 experiments (Sherman et al., 2013). Pächt et al. (2018) emphasized that boundary layer thickness
84 and turbulent structures are as important as mean shear stress and particle properties in determining
85 sediment initiation. As a result, conventional incipient motion models—calibrated in wind tunnels—
86 tend to overestimate the wind velocities required for natural transport. This discrepancy is also
87 crucial for predicting aeolian activity on extraterrestrial surfaces, such as Mars and Titan, where
88 boundary layer effects must be considered.

89 While previous studies have highlighted the importance of turbulent fluctuations, most have
90 focused on the velocity variability rather than explicitly resolving turbulent structures. For example,
91 Spies et al. (2000) and Wang and Zheng (2014) introduced periodic velocity fluctuations into steady
92 winds and observed enhanced transport at low velocities. Kok and Renno (2009) added turbulence
93 to logarithmic profiles and found that it altered the trajectories of small saltating particles
94 ($d_p < 250 \mu\text{m}$). Huang et al. (2020) further demonstrated the role of unsteady winds in aeolian
95 transport. However, such studies did not reproduce realistic turbulent structures and capture their
96 direct influence on particle motion. Dupont et al. (2013) numerically resolved turbulent structures
97 and reproduced near-surface aeolian streamers, while Wang et al. (2019) showed that streamers form
98 mainly in the near-wall regions of large-scale structures. More recently, Feng and Wang (2023)
99 compared transport statistics across boundary layers of different thicknesses, offering insights into
100 wind tunnel–field discrepancies, though their simulations used friction velocities

101 ($0.43 < u_* < 1.19 \text{ m} \cdot \text{s}^{-1}$) well above the fluid threshold ($u_*' = 0.21 \text{ m} \cdot \text{s}^{-1}$). Jin et al. (2024)
 102 investigated near-threshold transport and identified distinct entrainment mechanisms for rebound
 103 and impact thresholds, showing that particle energy variability influences transport patterns.
 104 Nonetheless, the role of boundary layer thickness in near-threshold aeolian sand transport remains
 105 poorly understood.

106 To address this gap, the present study builds upon the work of Jin et al. (2024) using three-
 107 dimensional large-eddy simulations coupled with a saltation model. We systematically examine how
 108 boundary layer flow conditions influence both the flow field and near-threshold sediment transport.
 109 Section 2 presents the governing equations, numerical methods, and simulation setup. Section 3
 110 reports the simulation results and analyzes the role of boundary layer thickness. The main findings
 111 are summarized in Section 4.
 112

113 2. Numerical Simulation Approach

114 The fluid in the boundary layer is assumed incompressible and without thermal exchange. The
 115 dimensionless governing equations are the filtered Navier–Stokes equations:

$$\frac{\partial u_i}{\partial x_i} = 0, \quad \frac{\partial u_i}{\partial t} + u_j \frac{\partial u_i}{\partial x_j} = -\frac{\partial p^*}{\partial x_i} + \nu \frac{\partial^2 u_i}{\partial x_j \partial x_j} + \frac{\partial \tau_{ij}}{\partial x_j} + f_i, \quad (1)$$

116 where $i=1,2,3$ denote streamwise, vertical, and spanwise directions, respectively, u_i is the
 117 filtered velocity, t is time, p^* is filtered kinematic pressure, ν is kinematic viscosity, τ_{ij} is
 118 sub-grid scale (SGS) stress, and $f_i = -1/(\Delta_x \cdot \Delta_y \cdot \Delta_z) \sum_{n=1}^{N_p} f_{Di}$ is the volume force exerted by
 119 particles, where $\Delta_x \cdot \Delta_y \cdot \Delta_z$ is grid volume, N_p is the total number of particles within the grid,
 120 and f_{Di} is the drag force.

121 Spatial discretization uses a second-order centered finite-difference scheme with a staggered
 122 grid in the vertical direction. Time integration applies a second-order Crank–Nicholson method.
 123 Further implementation details are available in Kim et al. (2002) and Zheng et al. (2020). The
 124 turbulent flow field is initiated by adding random perturbations to the mean laminar wind velocity
 125 profile. Periodic boundary conditions are imposed horizontally, with a stress-free condition at the
 126 top of the domain. At the bottom boundary, the integral wall model proposed by Yang et al. (2015)
 127 is employed due to its superior performance compared to other approaches (Jin et al., 2023). Sub-
 128 grid scale stress is represented using the scale-dependent dynamic model (Porté-Agel et al., 2000),
 129 consistent with Feng and Wang (2023) and Jin et al. (2024).

130 Particle trajectories are resolved individually in a Lagrangian framework. Particle velocity u_{pi}
 131 is given by:

$$m_p \frac{du_{pi}}{dt} = f_{Di} + m_p g \delta_{i2} = \frac{1}{2} C_{dp} A_p |u(x_p) - u_p| (u_i(x_{pi}) - u_{pi}) + m_p g \delta_{i2} \quad (2)$$

132 where m_p is particle mass, $C_{dp} = 24(1 + 0.15Re_p^{0.687}) / Re_p$ is the drag coefficient (Clift et al.,
 133 1978), $A_p = \pi d_p^2 / 4$ is the cross-sectional area of the particle, $Re_p = |u(x_p) - u_p| \cdot d_p / \nu$ is the
 134 particle Reynolds number, and $u(x_p)$ is the filtered fluid velocity at the particle location
 135 interpolated with a third-order Lagrange scheme.

136 Aerodynamic entrainment is calculated using the residual shear stress rules (Anderson and Haff,
 137 1991; Shao and Li, 1999): $N_a = (m_p \alpha_x u_\tau)^{-1} (\tau - \tau_t)$, where τ is the local resolved shear stress, τ_t
 138 is the threshold of aerodynamic entrainment (fluid threshold), u_τ is the friction velocity of sand-
 139 free flow, and α_x is an empirical coefficient. Liftoff velocity and angle distributions follow Jin et
 140 al. (2024), consistent with the numerical experiments of Jia and Wang (2021). In addition, a splash
 141 function is applied when particles impact the surface, accounting for both the rebound of incident
 142 particles and the ejection of bed particles (Anderson and Haff, 1991; Dupont et al., 2013). The
 143 rebound probability, as well as the velocity and angle distributions of rebounding particles, together
 144 with the number, velocity, and angular distributions of newly ejected particles, follow the model of
 145 Zheng et al. (2020). It is worth noting that, while the Discrete Element Method (DEM) can explicitly
 146 resolve particle-scale interactions and realistically capture collective effects (Jia and Wang, 2022;
 147 Tholen et al., 2023), the traditional splash function adopted in this study—based on static-bed,
 148 single-particle impact assumptions—serves as a parameterized approximation of complex particle-
 149 bed interactions under the condition of a large computational domain, even though more refined
 150 static-bed splash models are available (Lämmel et al., 2017; Comola and Lehning, 2017).

151 Bed particles are initially entrained into the boundary layer by fluid forces, after which the
 152 splash mechanism sustains the development of sand transport. To maintain periodicity, particles
 153 exiting the computational domain horizontally are reintroduced from the opposite boundary, while
 154 those escaping from the top boundary are re-injected into the flow with their vertical velocity
 155 reversed.

156 To examine the effect of boundary layer thickness (δ) on near-threshold transport, two cases
 157 were simulated with $\delta = 5.0 m$ and $10.0 m$. Results from a smaller domain ($\delta = 1.0 m$) partly
 158 draw on Jin et al. (2024). The computational domain dimensions are
 159 $(L_x \times L_y \times L_z) = (8\pi\delta \times \delta \times 2\pi\delta)$. Grids are uniform in the horizontal direction and stretched
 160 vertically using a hyperbolic tangent function with refinement near the wall ($y_1 = 0.012, 0.014 m$
 161 for $\delta = 5.0 m$ and $10.0 m$). For particle field post-processing, identical vertical grid resolution
 162 was applied to ensure comparability. Bed particles follow a slightly skewed Gaussian size
 163 distribution with a mean diameter of $200 \mu m$ (Zhu et al., 2019; Liu et al., 2022). Particle and air
 164 densities are $\rho_p = 2650 kg \cdot m^{-3}$ and $\rho = 1.2 kg \cdot m^{-3}$, giving a density ratio of 2208. The

165 α_x and τ_i values are consistent with Jin et al. (2024). Table 1 lists the simulation cases and key
 166 parameters.

167

168 Table 1. Bulk fluid velocity (u_b), saltation friction velocity (u_* , effective friction velocity
 169 considering particle feedback), Shields number ($\theta_* = u_*^2 / [(\rho_p / \rho - 1)gd_p]$), boundary layer
 170 thickness (δ), grid sizes in three directions ($N_x \times N_y \times N_z$), and sand transport rate (Q) for 16
 171 simulated cases with sediment transport.

| Cases | u_b ($m \cdot s^{-1}$) | u_* ($m \cdot s^{-1}$) | θ_* | δ (m) | $N_x \times N_y \times N_z$ | Q ($kg \cdot m^{-1} \cdot s^{-1}$) |
|-------|----------------------------|----------------------------|------------|--------------|-----------------------------|---|
| 1 | 2.90 | 0.10 | 0.0024 | 5.0 | 512×64×128 | 4.65×10^{-7} |
| 2 | 3.20 | 0.11 | 0.0028 | 5.0 | 512×64×128 | 4.36×10^{-6} |
| 3 | 3.40 | 0.12 | 0.0032 | 5.0 | 512×64×128 | 1.39×10^{-5} |
| 4 | 4.04 | 0.14 | 0.0043 | 5.0 | 512×64×128 | 2.09×10^{-4} |
| 5 | 5.30 | 0.18 | 0.0072 | 5.0 | 512×64×128 | 1.59×10^{-3} |
| 6 | 7.70 | 0.27 | 0.0168 | 5.0 | 512×64×128 | 8.69×10^{-3} |
| 7 | 10.30 | 0.38 | 0.0339 | 5.0 | 512×64×128 | 2.41×10^{-2} |
| 8 | 2.81 | 0.09 | 0.0018 | 10.0 | 768×64×192 | 2.69×10^{-7} |
| 9 | 3.00 | 0.10 | 0.0021 | 10.0 | 768×64×192 | 1.29×10^{-6} |
| 10 | 3.40 | 0.11 | 0.0026 | 10.0 | 768×64×192 | 1.91×10^{-5} |
| 11 | 3.70 | 0.12 | 0.0032 | 10.0 | 768×64×192 | 7.17×10^{-5} |
| 12 | 4.55 | 0.14 | 0.0043 | 10.0 | 768×64×192 | 3.71×10^{-4} |
| 13 | 6.45 | 0.20 | 0.0088 | 10.0 | 768×64×192 | 2.99×10^{-3} |
| 14 | 7.00 | 0.22 | 0.0106 | 10.0 | 768×64×192 | 4.22×10^{-3} |
| 15 | 8.15 | 0.25 | 0.0150 | 10.0 | 768×64×192 | 7.28×10^{-3} |
| 16 | 10.90 | 0.36 | 0.0291 | 10.0 | 768×64×192 | 1.80×10^{-2} |

172

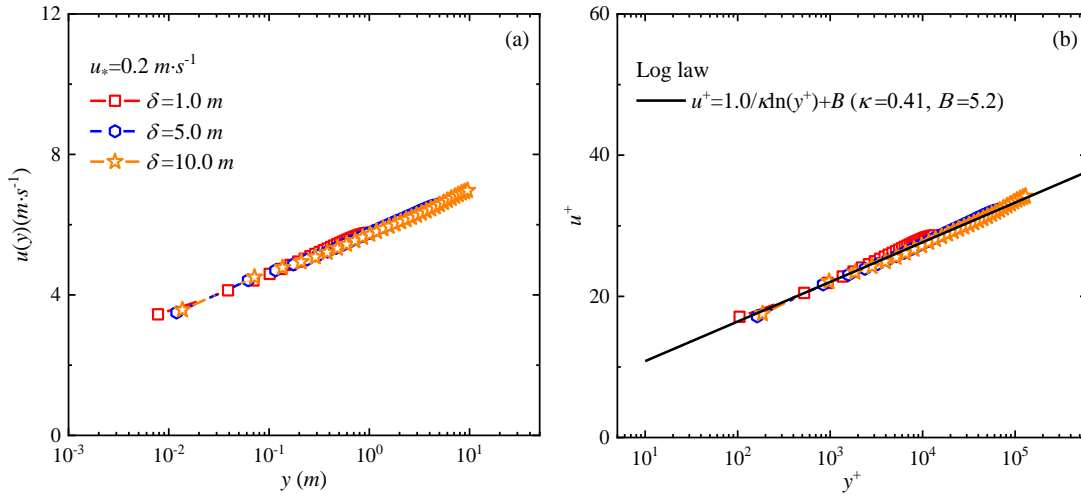
173 3. Results and Discussion

174 This section examines how boundary layer thickness influences near-threshold sand transport.
 175 It should be noted that the boundary layer thickness δ not only affects outer-layer structures and
 176 inner-outer interactions, but also acts through the friction Reynolds number $Re_\tau = u_*\delta / \nu$. Under
 177 the same friction velocity u_* and ν , a larger δ corresponds to a higher Re_τ , which supports
 178 larger-scale turbulent eddies and richer multi-scale interactions. Therefore, the boundary layer
 179 thickness effects observed in this study are essentially manifestations of Reynolds number effects
 180 under near-threshold transport conditions.

181 The simulations span wind velocities from the rebound threshold up to values exceeding the
 182 impact entrainment threshold. The rebound threshold in this study refers to the critical condition
 183 determined by observing the complete cessation of intermittent saltation motion. It is diagnosed
 184 from the simulation results by systematically reducing the wind velocity and observing the complete

185 cessation of all particle motion over a sufficiently long statistical period. Its physical essence is
 186 consistent with the critical Shields number defined by Pätz et al. (2020), which signifies whether
 187 sustained particle rebound can be maintained. It should be noted that the determination method
 188 differs from the one that estimates the threshold by extrapolating the continuous transport rate to
 189 zero. The impact entrainment threshold is identified as the point where the transport regime
 190 transitions from intermittent to continuous, corresponding to a marked change in the slope of the
 191 transport rate curve.

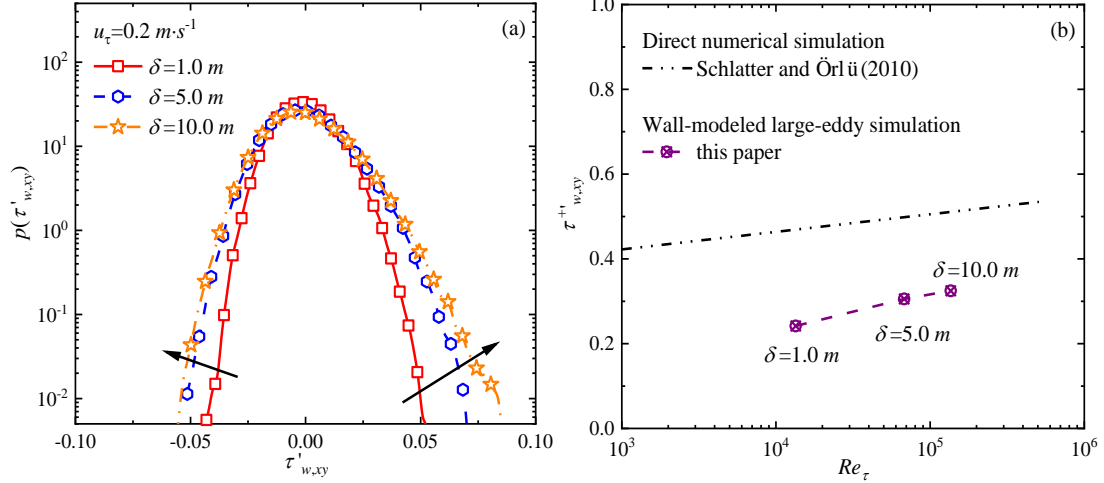
192 To reduce computational cost, each numerically resolved particle represents multiple physical
 193 particles (Dupont et al., 2013), with the representative ratio ranging from 50 to 2000 depending on
 194 boundary layer thickness and friction velocity. The analysis begins with mean wind velocity profiles
 195 and wall-shear stress fluctuations, followed by transport behavior and particle dynamics.



196
 197 Fig. 1. (a) Mean wind velocity profiles $u(y)$ for three boundary layer thicknesses ($\delta = 1.0, 5.0,$
 198 10.0 m); (b) inner-scale normalized profiles u^+ compared with the logarithmic law ($\kappa = 0.41$
 199 is the von Kármán constant and B is taken as 5.5 in the channel, $u_\tau = 0.21 \text{ m} \cdot \text{s}^{-1}$).

200

201 Fig. 1(a) shows mean wind velocity profiles for three boundary layer thicknesses at a fixed
 202 friction velocity, plotted in log-linear coordinates. Profiles overlap closely, with only minor
 203 differences at the first grid point for the smallest boundary layer. Near-wall velocities remain
 204 consistent across all cases, confirming that the first-grid-point height has a negligible influence.
 205 Normalizing the profiles using inner scales ($u^+ = u / u_\tau$, $y^+ = u_\tau y / \nu$) (Fig. 1(b)) shows excellent
 206 agreement with the logarithmic law, validating the simulated mean flow fields across boundary layer
 207 thicknesses.



208

209

210

211

212

213

214

215

216

217

218

219

220

221

222

223

224

225

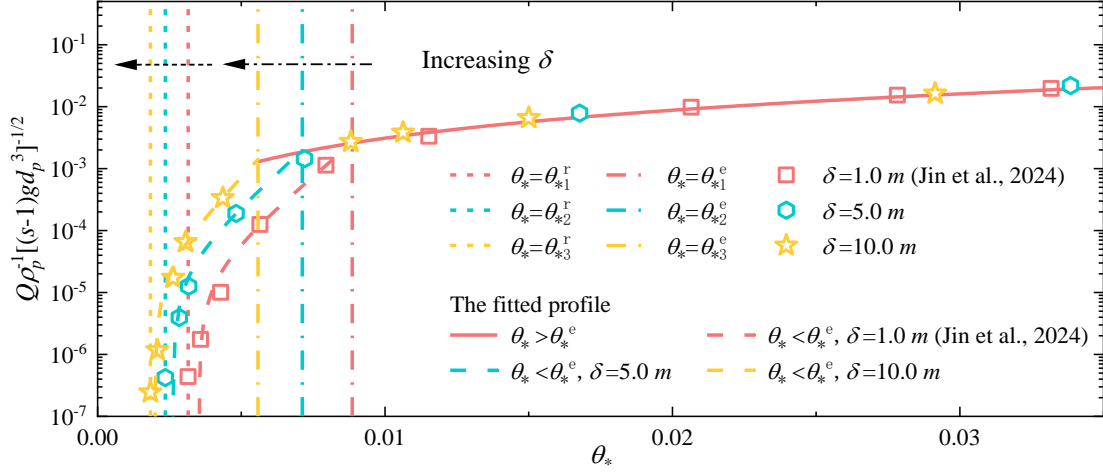
226

227

228

Fig. 2. (a) Probability density distributions and (b) standard deviations of wall-shear stress fluctuations $\tau'_{w,xy}$ for different boundary layer thicknesses ($\delta = 1.0, 5.0, 10.0 \text{ m}$). The direct numerical simulation results of Schlatter and Örlü (2010) are given by the double-dash-dotted line.

Particle liftoff is initiated by instantaneous high shear stresses or local pressure imbalances generated by turbulent fluctuations. Boundary layer thickness influences the velocity threshold for entrainment by modulating near-wall turbulent structures and the resulting wall-shear stress field (Lu et al., 2005; Pächt et al., 2018). Fig. 2(a) shows the probability density distributions of wall-shear stress fluctuations under the same free-stream wind velocity. The simulations reveal clear differences across boundary layer thicknesses. As the boundary layer increases, the probability densities at both tails of the distribution—especially for positive fluctuations above the mean—also increase. This trend arises because the boundary layer thickness constrains the largest turbulent scales (Pächt et al., 2018). A thicker boundary layer supports a broader range of turbulent scales, producing stronger instantaneous wall-shear stresses. When the boundary layer thickness increases fivefold (from 1.0 m to 5.0 m), the fluctuation amplitude rises markedly, but further increases lead to a slower rate of growth. Fig. 2(b) compares the standard deviation of wall-shear stress fluctuations with the direct numerical simulation results of Schlatter and Örlü (2010). The lower values obtained here reflect the use of wall-modeled large-eddy simulations with relatively coarse grid resolution. Despite this, the Reynolds number dependence across different boundary layer thicknesses is well captured.



229

230

231

232

233

234

235

236

237

238

239

240

241

242

243

244

245

246

247

248

249

250

251

252

253

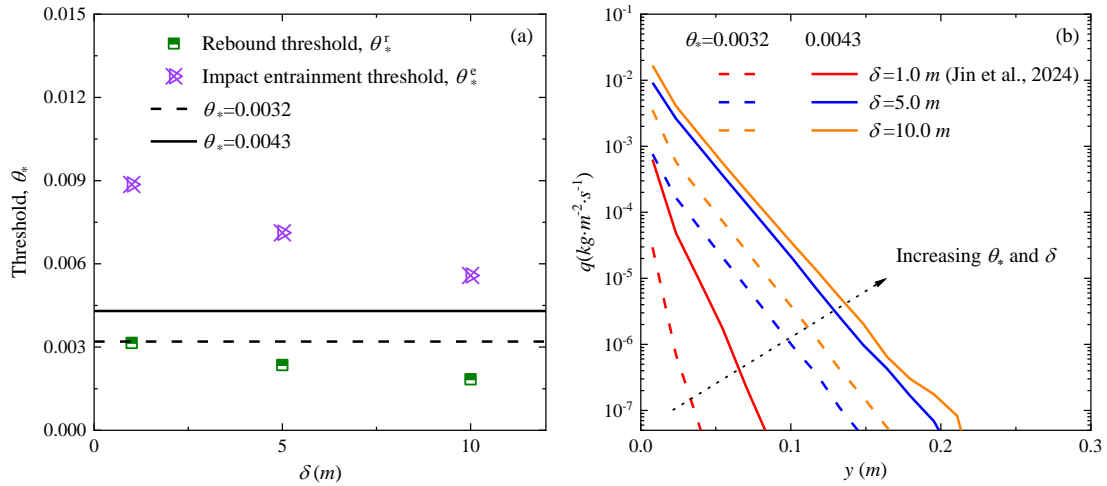
254

Fig. 3. Simulated sand transport rates $Q\rho_p^{-1}[(s-1)gd_p^3]^{-1/2}$ under different boundary layer thicknesses ($\delta = 5.0, 10.0 \text{ m}$) and wind velocities, where s is the density ratio of particle and air.

Large-scale turbulent structures carry significant energy and Reynolds stress (Guala et al., 2006; Balakumar and Adrian, 2007), thereby enhancing energy transfer (Marusic et al., 2010; Serafimovich et al., 2011). The influence of boundary layer thickness on these large structures can further affect particle motion in sand-laden flows. Under simulated conditions with $\delta = 1.0 \text{ m}$, Jin et al. (2024) reported that above the impact entrainment threshold (θ_*^e), the time-averaged sand transport rate scales shear stress raised to the power of 1.5 (the same as Bagnold (1941) and White (1979), whereas below θ_*^e , it varies exponentially with shear stress. As shown in Fig. 3, the simulated sand transport rates across different boundary layer thicknesses and dimensionless wind velocities follow the same trend, with fitted curves yielding a high correlation coefficient (R^2). However, the threshold wind velocities depend strongly on the boundary layer thickness. For example, the impact entrainment thresholds required for sustained continuous transport are $\theta_{*2}^e = 0.00712$ and $\theta_{*3}^e = 0.00558$ for $\delta = 5.0 \text{ m}$ and 10.0 m , respectively (dot-dashed lines in Fig. 3). These correspond to impact threshold wind velocities (u_*^e) of 0.18 and $0.16 \text{ m} \cdot \text{s}^{-1}$, equal to 0.58 and 0.52 times the fluid threshold ($u_*^f = 0.31 \text{ m} \cdot \text{s}^{-1}$). Similarly, rebound thresholds were $\theta_{*2}^r = 0.00235$ and $\theta_{*3}^r = 0.00184$ (dashed lines in Fig. 3), corresponding to rebound threshold wind velocities (u_*^r) of 0.1 and $0.09 \text{ m} \cdot \text{s}^{-1}$, or 0.32 and 0.29 times the fluid threshold.

For a particle size of $200 \mu\text{m}$, the threshold coefficient in a fluctuating flow field is about 1.5 times that in the time-averaged flow (Li et al., 2020a). Based on the entrainment threshold of $u_*^f = 0.21 \text{ m} \cdot \text{s}^{-1}$ obtained from wind tunnel experiments, the rebound thresholds are 47.6% and 42.9% of this value, respectively. Field studies also indicate that transport may occur when the friction velocity is just 50% of the wind-tunnel threshold (Rasmussen and Sørensen, 1999). Given

255 measurement uncertainties and the difficulty detecting particles close to the bed (Jin et al., 2021),
 256 the thresholds under field conditions may be even lower than those estimated here. Fig. 4(a) further
 257 shows that both θ_*^e and θ_*^r decrease with increasing boundary layer thickness, with the decline
 258 in θ_*^e more pronounced. This is consistent with the observation by Williams et al. (1994) that the
 259 fluid threshold decreases as turbulence intensifies (effectively equivalent to increasing boundary
 260 layer height). Increasing the boundary layer thickness significantly alters the turbulence structure
 261 (Li et al., 2020a; Zhang et al., 2022), which modifies the instantaneous probability of exceeding
 262 the threshold. This is precisely the physical mechanism underlying the threshold reduction.



263
 264 Fig. 4. (a) Rebound θ_*^r and impact entrainment θ_*^e thresholds and (b) sediment transport
 265 intensity q for different boundary layer thicknesses (Data for $\delta = 1.0$ m taken from Jin et al.
 266 (2024)). The dashed line represents $\theta_* = 0.0032$, and the solid line represents $\theta_* = 0.0043$. The
 267 color corresponds to different boundary layer thicknesses. The black dotted arrow in (b) represent
 268 the increase of boundary layer thickness and wind velocity.

269
 270 Notably, when $\theta_* > \theta_*^e$, the differences in sand transport rates across varying boundary layer
 271 thicknesses become negligible. In contrast, when $\theta_* < \theta_*^e$, the sand transport rate scales with the
 272 boundary layer thickness and rises sharply with increasing wind velocity (Rasmussen and Sørensen,
 273 1999). For example, at $\theta_* = 0.0043$, the transport rates for $\delta = 5.0$ m and 10.0 m are 19 and
 274 33 times that for $\delta = 1.0$ m, respectively; at $\theta_* = 0.0032$, the corresponding factors increase to
 275 29 and 149, demonstrating that the influence of boundary layer thickness is more pronounced at
 276 lower wind velocities. This aligns with the observation made by Williams et al. (1990) that turbulent
 277 fluctuations promote entrainment. However, limited by the dimensions of the wind tunnel, the
 278 boundary layer thickness in their experiments typically ranges from centimeters to decimeters
 279 (corresponding to Re_τ on the order of 10^3 – 10^4), representing a classic laboratory scale. By
 280 systematically extending δ from 1.0 m to 10.0 m in our simulations (with Re_τ reaching

281 $\sim 10^5$), we have directly bridged the gap between laboratory scales and natural atmospheric scales,
282 where δ is commonly on the order of hundreds of meters.

283 These findings suggest that in real field conditions, sediment transport rates may be higher and
284 threshold wind velocities lower than predicted in conventional wind tunnels. Feng and Wang (2023)
285 reported a similar trend, observing that sediment transport rates increase with boundary layer
286 thickness at wind velocities ($\theta_* > 0.15$, $u_* > 0.8 \text{ m} \cdot \text{s}^{-1}$ in their study) well above the near-
287 threshold regime considered in this study. This implies that the effect of boundary layer thickness
288 on sediment flux depends on the wind velocity and the dominant particle entrainment mechanism.

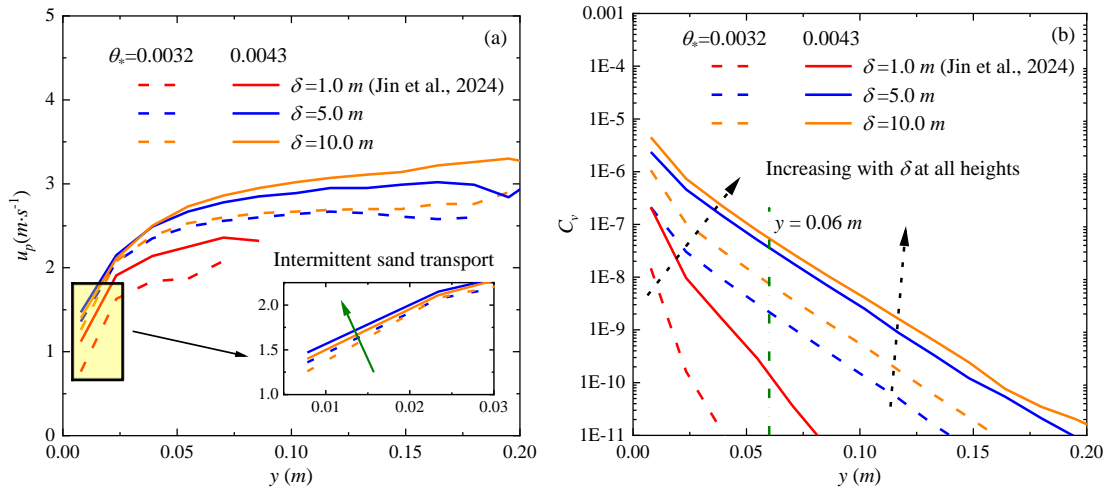
289 Specifically, at wind velocities below the impact entrainment threshold (θ_*^e), thicker boundary
290 layers generate higher instantaneous wall-shear stresses, enhancing fluid-driven particle flux and
291 increasing the sand transport rate. When wind velocities far exceed the impact entrainment threshold
292 ($\theta_* > 21 \theta_{*2}^e$ or $> 27 \theta_{*3}^e$ according to Feng and Wang (2023)), splash-driven entrainment
293 dominates, and the sand transport flux becomes approximately proportional to the boundary layer
294 thickness. In the transitional wind velocity regime between these limits, both fluid- and splash-
295 driven processes are relatively insensitive to boundary layer thickness, resulting in minimal
296 variation in transport rates.

297 Sediment transport intensity ($q(y) = \sum m_p \bar{u}_p / (L_x \times \Delta_y \times L_z)$), which is defined as the
298 horizontal sand mass flux per unit height interval, serves as a key metric linking the microscopic
299 mechanisms of aeolian sand movement—such as particle entrainment and collisions—to
300 macroscopic outcomes, including the overall sediment transport rate. Using the same grid resolution
301 (grid size of $\delta = 1.0 \text{ m}$), Fig. 4(b) shows how sediment transport intensity varies with height for
302 different boundary layer thicknesses ($\delta = 5.0, 10.0 \text{ m}$) and dimensionless shear velocities
303 ($\theta_* = 0.0032, 0.0043$). For comparison, simulation results for $\delta = 1.0 \text{ m}$ (Jin et al., 2024) are also
304 included to highlight the combined effects of wind velocity and boundary layer thickness. All
305 profiles exhibit an exponential decay with increasing height.

306 As illustrated in Fig. 4(a), the selected wind velocities ($\theta_* = 0.0032, 0.0043$) are above the
307 rebound threshold but below the impact entrainment threshold for all three boundary layer
308 thicknesses, indicating that sediment transport occurs intermittently under these conditions. As both
309 wind velocity and boundary layer thickness increase, the sediment transport intensity rises across
310 all heights, with differences becoming more pronounced at greater heights. The effect of boundary
311 layer thickness is particularly significant at lower wind velocities. For instance, at a height of
312 $y = 0.04 \text{ m}$, the sediment transport intensity for $\delta = 5.0 \text{ m}$ and 10.0 m increases by
313 approximately 1000 and 3000 times, respectively, relative to $\delta = 1.0 \text{ m}$ at $\theta_* = 0.0032$. At
314 $\theta_* = 0.0043$, the corresponding increases are about 100 and 150 times, indicating that the influence

315 of boundary layer thickness diminishes as wind velocity increases. Importantly, the variations in
 316 sediment transport intensity due to boundary layer thickness at this height are far larger than those
 317 observed in the total transport rate, since the sediment transport intensity for $\delta = 1.0\text{ m}$ is
 318 relatively low and contributes only minimally to the overall flux.

319 Fig. 5(a) shows the vertical profile of mean horizontal particle velocity. Unlike continuous
 320 transport conditions—where wind velocities exceed the impact entrainment threshold and thicker
 321 boundary layers generally result in faster particle movement at the same wind velocity (Feng and
 322 Wang, 2023)—the relationship under sub-threshold conditions is non-monotonic. At different wind
 323 velocities, particle velocity for $\delta = 1.0\text{ m}$ is lower than for $\delta = 5.0\text{ m}$, but shows little change
 324 when the boundary layer thickness increases further to $\delta = 10.0\text{ m}$. As wind velocity rises, the
 325 velocity difference between $\delta = 1.0\text{ m}$ and $\delta = 5.0\text{ m}$ or 10.0 m diminishes. Simulation
 326 results for $\delta = 5.0\text{ m}$ and 10.0 m also demonstrate that near-wall particle velocity is
 327 proportional to wind velocity (see inset of Fig. 5(a)), confirming that sediment transport remains
 328 intermittent when $\theta_* < 0.0043$ (Jin et al., 2024). However, greater boundary layer thickness leads
 329 to smaller velocity variations across different wind velocities under thicker boundary layers.

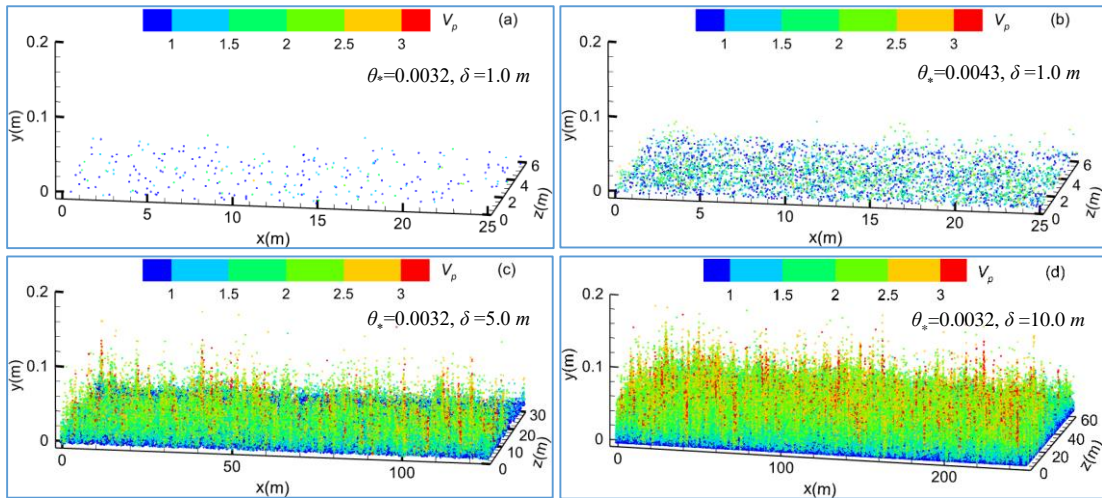


330
 331 Fig. 5. Vertical profiles of (a) mean horizontal particle velocity u_p and (b) particle volume
 332 fraction C_v for different boundary layer thicknesses ($\delta = 5.0, 10.0\text{ m}$). The dashed line
 333 represents $\theta_* = 0.0032$, and the solid line represents $\theta_* = 0.0043$. The color corresponds to
 334 different boundary layer thicknesses. The green arrow in (a) and the black dotted arrow in (b)
 335 represent the increase of boundary layer thickness and wind velocity.

336
 337 Feng and Wang (2023) observed that particle volume fraction increases with boundary layer
 338 thickness only in regions far from the wall (e.g., $y > 0.06\text{ m}$ when $\theta_* = 0.0427$). In contrast, the
 339 present results show that under the same wind velocity, particle volume fraction is proportional to
 340 boundary layer thickness across all heights (Fig. 5(b)). This discrepancy arises due to the

341 predominance of fluid-driven particle entrainment under low wind velocities rather than splash
 342 events. These fluid-driven particles move at lower velocities, and only a small fraction gains
 343 sufficient energy to reach the saltation layer. Consequently, near-wall particle concentration exhibits
 344 a strong dependence on boundary layer thickness. Supporting this, Jin et al. (2024) showed for
 345 $\delta = 1.0 \text{ m}$ that when $\theta_* = 0.0032$ (very close to the rebound threshold), the transport flux is
 346 almost entirely carried by fluid-driven particles. Because such particles have much lower energy
 347 than splash-entrained ones, their flux decays rapidly with height. As wind velocity and boundary
 348 layer thickness increase—where a thicker boundary layer at the same wind velocity corresponds to
 349 a larger argin above the rebound threshold—the decay rate of particle flux with height decreases
 350 progressively.

351 As wind velocity approaches the rebound threshold, the height of particle saltation decreases.
 352 To illustrate how particle distributions vary with wind velocity and boundary layer thickness, Fig. 6
 353 shows instantaneous particle fields at a representative moment after the aeolian sand flow has
 354 reached a steady state for $\delta = 1.0 \text{ m}$ ($\theta_* = 0.0032, 0.0043$), $\delta = 5.0 \text{ m}$ ($\theta_* = 0.0032$), and
 355 $\delta = 10.0 \text{ m}$ ($\theta_* = 0.0032$). Particle colors denote velocity, and each plotted particle represents 50
 356 actual particles. For $\delta = 1.0 \text{ m}$ at $\theta_* = 0.0032$, the maximum saltation height is about 0.03 m
 357 (roughly 150 particle diameters), indicating weak sand transport (Fig. 6(a)). Particle motion is
 358 confined to creep or short saltation near the wall, with particle detachment relying primarily on
 359 turbulent fluctuations rather than interparticle collisions. As wind velocity increases ($\theta_* = 0.0043$,
 360 Fig. 6(b)), particle motion intensifies, velocities rise, and the aeolian sand flow develops more
 361 rapidly with increasing boundary layer thickness. Under $\delta = 10.0 \text{ m}$, the maximum saltation
 362 height approaches 0.2 m . Statistical results confirm that at higher wind velocities, increases in
 363 flux are dominated by higher particle concentrations (Fig. 5).



364

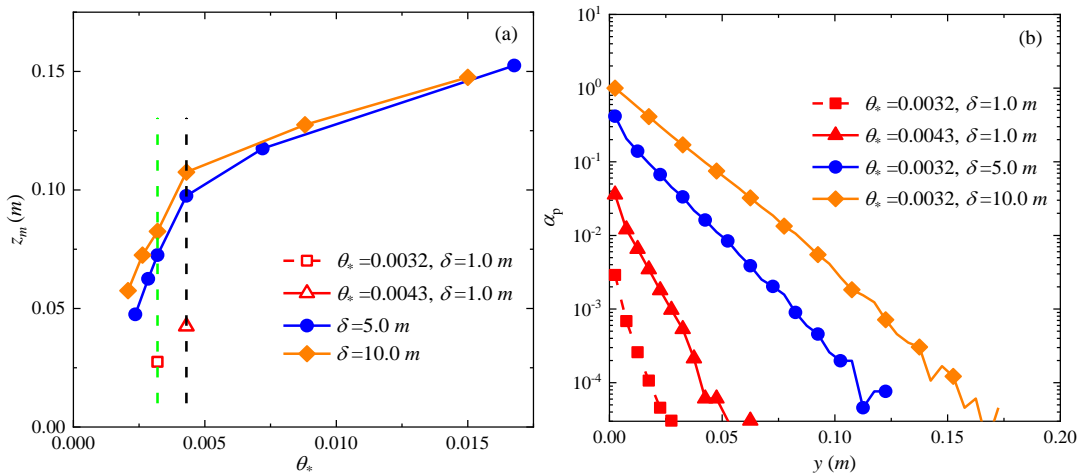
365 Fig. 6. Instantaneous particle fields V_p for different boundary layer thicknesses

366 ($\delta = 1.0, 5.0, 10.0 \text{ m}$) and wind velocities: (a) $\theta_* = 0.0032$, $\delta = 1.0 \text{ m}$; (b) $\theta_* = 0.0043$,
 367 $\delta = 1.0 \text{ m}$; (c) $\theta_* = 0.0032$, $\delta = 5.0 \text{ m}$; (d) $\theta_* = 0.0032$, $\delta = 10.0 \text{ m}$, where data for
 368 $\delta = 1.0 \text{ m}$ come from Jin et al. (2024). The resultant velocity V_p is equal to the square root of
 369 the sum of the squares of the velocities in the three directions.

370

371 The saltation layer height z_m was also extracted (Fig. 7(a)), defined as the elevation below
 372 which 99.5% of the total mass flux occurs (Dupont et al., 2013). At wind velocities of $\theta_* = 0.0032$
 373 and 0.0043 , the saltation layer thickness for $\delta = 10.0 \text{ m}$ is approximately 3.0 and 2.5 times
 374 greater than for $\delta = 1.0 \text{ m}$, respectively. As wind velocity increases further, the differences among
 375 boundary layer thicknesses diminish, especially for $\delta = 5.0 \text{ m}$ and $\delta = 10.0 \text{ m}$.

376 To quantify the non-uniformity of particle distributions, we define the particle spatial
 377 occupancy (α_p) as the ratio of grid cells containing particles to the total number of grid cells. Using
 378 the instantaneous particle fields shown in Fig. 6, Fig. 7(b) presents the vertical variation of α_p
 379 under different conditions at the same grid resolution. The results show that α_p decays
 380 exponentially with increasing height, reflecting its close relationship to the vertical distribution of
 381 particle volume fraction. Near the wall, α_p for $\delta = 10.0 \text{ m}$ approaches 1, indicating nearly
 382 complete grid-cell occupancy. Under the same wind velocity, α_p for $\delta = 5.0 \text{ m}$ decreases to ~
 383 0.4, indicating spatial heterogeneity in particle distribution, while for $\delta = 1.0 \text{ m}$, α_p falls
 384 sharply to 0.003, signifying strong spatial variability with particles confined to localized regions
 385 of the flow.



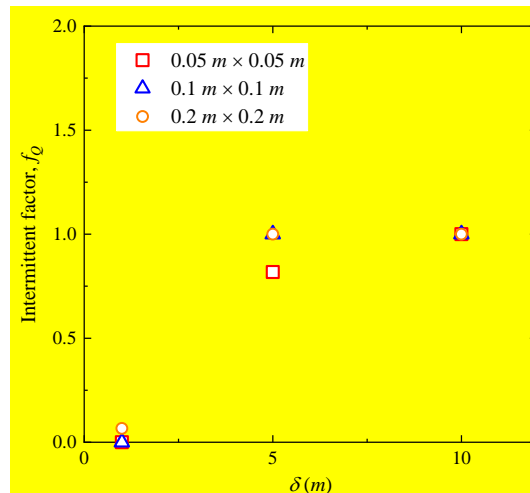
386

387 Fig. 7. (a) Saltation layer height z_m and (b) particle spatial occupancy α_p for different
 388 boundary layer thicknesses ($\delta = 5.0, 10.0 \text{ m}$) and wind velocities. The green and black dashed
 389 lines in (a) are auxiliary lines for $\theta_* = 0.0032$ and 0.0043 .

390

391 Increasing boundary layer thickness markedly enhances energy transfer between the turbulent

392 flow and the particle phase. Large-scale vortices in thicker boundary layers carry greater energy and
 393 persist longer, which promotes more effective and sustained particle lifting, resulting in both vertical
 394 and horizontal dispersion and thus a more uniform distribution and significantly higher α_p values.
 395 Moreover, the effect of boundary layer thickness on α_p increases with increasing height above the
 396 wall (Fig. 7(b)).



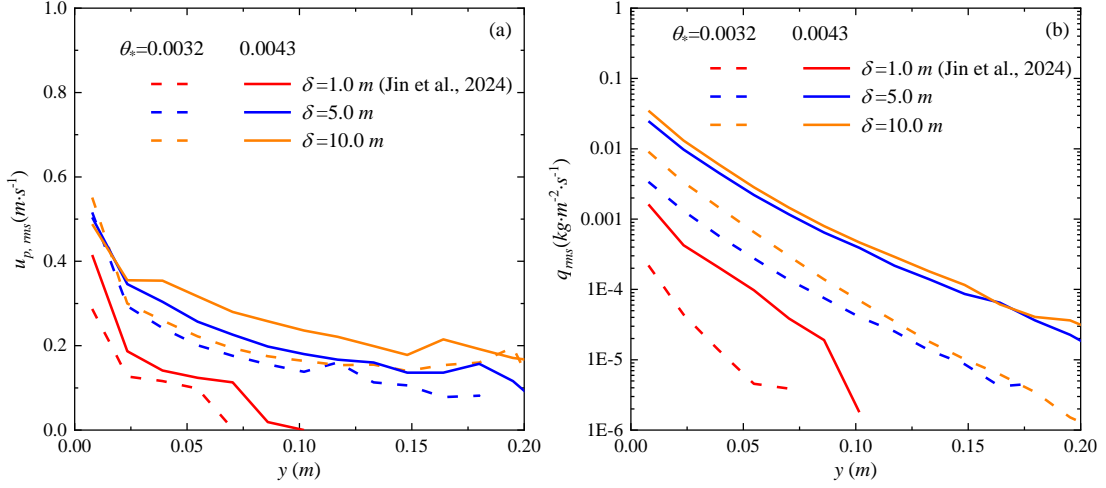
397

398 Fig. 8. Fraction of time f_Q for which saltation is in an "active" state under different boundary

399 layer thicknesses ($\theta_s = 0.0032$).

400

401 Furthermore, taking the near-threshold wind velocity ($\theta_s = 0.0032$) as an example, we selected
 402 three different domains (all centered within the computational domain): $0.05\text{ m} \times 0.05\text{ m}$,
 403 $0.1\text{ m} \times 0.1\text{ m}$, and $0.2\text{ m} \times 0.2\text{ m}$. Within these finite horizontal domains, we present the fraction
 404 of time f_Q for which saltation is in an "active" state over a given analysis time window Δt (2 s),
 405 as defined by Martin and Kok (2018), based on a total time series exceeding 60 s (Fig. 8). It can
 406 be seen that for the thin boundary layer ($\delta = 1.0\text{ m}$), f_Q approaches zero in any of the finite
 407 domains, whereas for the thick boundary layers ($\delta = 5.0\text{ m}$ and 10.0 m), f_Q is close to 1 in all
 408 finite domains. This demonstrates that, in near-threshold large-scale simulations, f_Q is severely
 409 constrained by the stark dichotomy of transport states. Therefore, in the present study, α_p is
 410 adopted to compare the tendency of particle transport toward spatial dispersion or clustering under
 411 different boundary layer thicknesses — precisely the kind of global structural information that the
 412 spatiotemporal metric f_Q is inherently unable to capture.



413

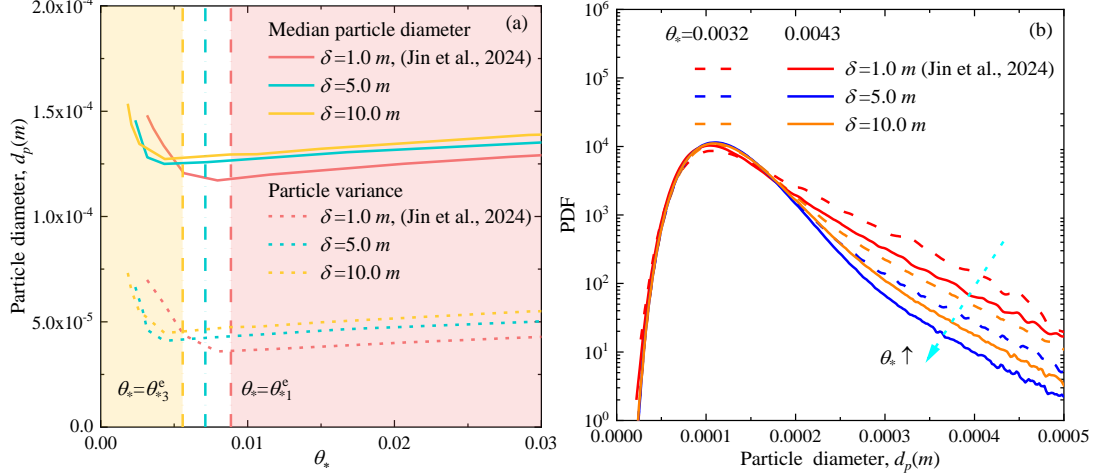
414 Fig. 9. Vertical profiles of (a) particle velocity $u_{p,rms}$ and (b) mass flux q_{rms} fluctuations for
 415 different boundary layer thicknesses ($\delta = 5.0, 10.0 \text{ m}$). The dashed line represents $\theta_* = 0.0032$,
 416 and the solid line represents $\theta_* = 0.0043$. The color corresponds to different boundary layer
 417 thicknesses.

418

419 Fig. 9 presents the vertical profiles of particle velocity and mass flux fluctuations. Even when
 420 the boundary layer thickness increases to 5.0 m and 10.0 m , the peak of particle velocity
 421 fluctuations remains located in the near-wall region. This near-wall concentration of fluctuations
 422 can markedly intensify wind erosion under low wind velocity conditions. It also reinforces the
 423 prevalence of the intermittent transport regime, dominated by fluid-driven entrainment, which
 424 differs from the continuous saltation dominated by splash-driven entrainment, where the velocity
 425 fluctuation peak typically occurs several centimeters above the bed (Feng and Wang, 2023). Across
 426 all simulated wind velocities, increasing the boundary layer thickness from 1.0 m to 5.0 m
 427 significantly amplifies the near-wall velocity fluctuation peak, a phenomenon closely related to the
 428 intensification of outer large-scale structures and their influence on the inner region (Smits et al.,
 429 2011). However, further increases to 10.0 m produces little additional change, suggesting a
 430 gradual transition toward splash-driven entrainment. Differences in velocity fluctuations associated
 431 with boundary layer thickness become more apparent only at higher elevations above the wall.

432

433 Mass flux fluctuations near threshold also differ from those in continuous transport. As shown
 434 in Fig. 9(b), as the boundary layer thickness increases, the magnitude of transport rate fluctuations
 435 rises but the incremental effect diminishes, particularly at higher wind velocities. Consequently, the
 436 influence of boundary layer thickness on mass flux fluctuations weakens as wind velocity increases.
 437 This behavior mirrors the response of the mean sediment transport rate, reflecting the fact that as
 438 wind velocity approaches the splash-driven entrainment threshold, both fluid- and splash-driven
 processes become less sensitive to variations in boundary layer thickness.



439

440

441

442

443

444

445

446

447

448

449

450

451

452

453

454

455

456

457

458

459

460

461

462

463

464

Fig. 10 (a) Mean and variance, and (b) probability density distribution of particle diameter d_p for different boundary layer thicknesses ($\delta = 5.0, 10.0$ m) as a function of wind velocity. The median particle diameter is represented by solid lines, and the variance of particle diameter is represented by dashed lines in (a). The line types and colors in (b) are consistent with those in Figs. 5 and 9. The arrows in (b) indicate that as the wind velocity increases, the probability density of large particles (those with larger diameters) decreases.

Under conditions with boundary layer thicknesses $\delta = 5.0, 10.0$ m (Fig. 10(a)), the variation of particle diameter parameters reveals two distinct regimes. When wind velocity is below the impact entrainment threshold (θ_*^c), both the mean and variance of airborne particle diameter decrease with increasing θ_* . In contrast, once wind velocity exceeds θ_*^c , both parameters become proportional to θ_* , consistent with the conclusions drawn for $\delta = 1.0$ m and supporting the validity of defining the critical threshold based on transport rate. At lower wind velocities, the relationship between mean and variance differs across boundary layer thicknesses: $d_{p, \delta=1.0 m} > d_{p, \delta=5.0 m} > d_{p, \delta=10.0 m}$. Conversely, thicker boundary layer thicknesses result in greater mean and variance. The simulation results indicate the existence of two critical Shields numbers: $\theta_{*1} = 0.003$ and $\theta_{*2} = 0.005$. The shift in the particle statistics relationship corresponds to θ_{*1} when comparing $\delta = 10.0$ m with $\delta = 5.0$ m, and to θ_{*2} when comparing $\delta = 5.0, 10$ m with $\delta = 1.0$ m. For wind velocities of $\theta_* = 0.0032$ and 0.0043 , lying between these two critical values, the relationship between mean and variance shifts accordingly: $d_{p, \delta=1.0 m} > d_{p, \delta=10.0 m} > d_{p, \delta=5.0 m}$, as also confirmed by the probability density distributions in Fig. 10(b).

As wind velocity increases (θ_* rising from 0.0032 to 0.0043), the probability of entraining larger particles decreases because both $\theta_* = 0.0032$ and 0.0043 remain below θ_*^c , meaning that fluid-driven entrainment still dominates particle transport. Under these conditions, the enhanced near-wall transport flux induces a reduction in local wind velocities due to particle loading

465 (Jin et al., 2021), which further suppresses the fluid entrainment of larger particles.

466

467 **4. Discussion and Conclusions**

468 Unlike atmospheric stability (convective/stable conditions), which modify the generation
469 mechanisms and energy distribution patterns of turbulence, the boundary layer thickness not only
470 constrains the maximum possible scale of vortical structures in turbulent motion, but also affects
471 the near-wall turbulence characteristics through the interaction between the inner-outer interactions
472 (Guala et al., 2006; Marusic et al., 2010). Increasing δ corresponds to an expansion of the flow
473 domain in the vertical direction, allowing for the generation and development of larger-scale, more
474 energetic coherent structures. By fixing other flow parameters (the kinematic viscosity, the mean
475 wall friction velocity, the boundary conditions, and the manner in which the inflow turbulence is
476 initialized), this study highlights the influence of boundary layer thickness in modulating near-
477 threshold aeolian sediment transport, a process characterized by high intermittency. A thicker
478 boundary layer supports large-scale coherent structures, such as low-speed streaks or streamwise
479 vortex pairs. These structures induce high instantaneous shear stresses in the near-wall region. Even
480 when the mean shear stress is low, once this instantaneous stress exceeds the fluid threshold, it can
481 trigger localized burst-like particle motion, thereby dominating the intermittent transport behavior.

482 Recognizing that traditional models, often assuming steady, continuous sediment transport
483 governed by a single threshold (Kawamura, 1951; White, 1979; Creyssels et al., 2009), fail to
484 capture near-threshold behavior, this research addresses a critical knowledge gap. The primary
485 objective is to systematically elucidate how different boundary layer conditions influence the
486 turbulent flow field and the resulting particle entrainment and transport mechanisms near threshold.
487 To achieve this, the study employs the three-dimensional large-eddy simulation coupled with a
488 Lagrangian saltation model, aiming to provide a mechanistic understanding of wind tunnel-field
489 discrepancies.

490 Increasing boundary layer thickness enhances extreme values in wall-shear stress fluctuations.
491 As a result, both the impact entrainment threshold (θ_*^e or u_*^e) and the rebound threshold (θ_*^r or
492 u_*^r) decrease. For thick boundary layers ($\delta = 5.0\ m$ and $10.0\ m$), the rebound threshold wind
493 velocity can drop below 50% of values typically observed in conventional wind tunnel experiments.
494 Sediment transport responds differentially to wind velocity: at very low wind velocities ($\theta_* < \theta_*^e$
495 $< \theta_*^e$), transport increases markedly with thickness under fluid-driven entrainment; at high wind
496 velocities ($\theta_* > 21\ \theta_{*2}^e$ or $> 27\ \theta_{*3}^e$), it scales proportionally with thickness under splash-driven
497 entrainment; and at intermediate wind velocities, the effect is negligible. Near-bed particle velocity,
498 concentration, saltation height, and airborne particle diameter all increase with boundary layer

499 thickness, accompanied by reduced variability and more uniform spatial distributions.

500 A thicker boundary layer accommodates a broader range of turbulent scales, fostering stronger,
501 large-scale coherent structures that generate more extreme instantaneous stress events (Pächt et al.,
502 2018). This enhanced turbulence facilitates particle entrainment at lower mean wind velocities,
503 which also explains why the rebound threshold can be less than half the typical wind-tunnel value
504 (Rasmussen and Sørensen, 1999). Notably, the impact entrainment threshold exhibits a more
505 pronounced reduction, implying that sustaining continuous transport becomes feasible at relatively
506 lower velocities as boundary layer thickness increases. Furthermore, the dependence of sand
507 transport on boundary layer thickness reveals distinct regimes: at low winds, enhanced turbulent
508 fluctuations directly loft more particles, while at high winds, the system transitions to a splash-
509 dominated regime where transport capacity scales with the thicker boundary layer (Feng and Wang,
510 2023).

511 Thicker boundary layers promote more energetic large-scale turbulent structures that
512 effectively lift and disperse particles, leading to a more uniform distribution and reduced variability.
513 This mechanism explains previous field observations of longer and more persistent "streamers"
514 (Baas and Sherman, 2005; Sherman et al., 2013). Unlike the findings of Feng and Wang (2023),
515 which showed increased concentration only away from the wall, our results reveal the unique nature
516 of the near-threshold, fluid-entrainment-dominated regime. The observed reversal in particle size
517 trend is due to the shift from fluid-driven to splash-driven entrainment.

518 Convective boundary layers can reach thicknesses of $1-2\text{km}$, neutral boundary layers are
519 typically on the order of hundreds of meters, and stable boundary layers may contract to tens of
520 meters. The range of thicknesses simulated in this study precisely spans the transitional interval
521 from typical wind tunnel scales (approximately 0.1m) to natural atmospheric scales ($>100\text{m}$),
522 providing a crucial mechanistic explanation for understanding the systematic differences in
523 sediment transport thresholds and rates between wind-tunnel and field observations. Although this
524 study reveals the significant influence of boundary layer thickness on near-threshold aeolian
525 sediment transport, several issues require further investigation in the future, such as a thicker
526 boundary layer (closer to realistic atmospheric conditions) and a broader particle size distribution
527 to clarify the underlying mechanisms systematically. The current model does not account for
528 multiphysical processes, such as interparticle collisions, electrostatic interactions, or humidity
529 effects, which significantly influence the entrainment and transport of fine particles in natural
530 environments. A logically crucial and necessary step is to adopt the CFD–DEM framework—under
531 conditions that can resolve large-scale flow fields while incorporating realistic particle–particle and
532 particle–bed interactions—to verify, refine, and extend the findings obtained in this study based on

533 a macroscopic parameterized model. What's more, spectral methods or higher-order numerical
534 schemes will also be a key direction for future improvement.

535 Our findings fundamentally shift how the atmospheric boundary layer should be viewed in dust
536 emission modeling. By demonstrating that thicker boundary layers can halve the entrainment
537 thresholds and alter particle size distributions, we provide the mechanistic basis for the known
538 discrepancy between wind-tunnel models and field observations. This implies that current climate
539 models likely underestimate dust emissions. Integrating boundary layer thickness into dust emission
540 schemes is therefore critical for accurate simulation of aerosol radiative forcing, cloud processes,
541 and the evolution of arid landscapes in a changing climate.

542

543 *Data availability.* The data that support the findings of this study are available in the Figshare
544 repository (<https://doi.org/10.6084/m9.figshare.30245776>). Additional data related to this paper and
545 the codes may be requested from the authors.

546

547 *Author contributions.* Lifeng Zhou designed and organized the research and its approach. Ting Jin
548 carried out the simulation, analyzed the results, wrote the manuscript and carefully modified the
549 manuscript. All authors contributed to the paper.

550

551 *Competing interests.* The authors declare that they have no conflict of interest.

552

553 *Acknowledgements.* This work was funded by the National Natural Science Foundation of China
554 (No. 12202170) and the Yunnan Fundamental Research Projects (No. 202301AT070164).

555

556 **References**

557 Almeida, M. P., Andrade, J. S., Herrmann, H. J.: Aeolian transport layer, *Physical Review Letters*, 96,
558 018001, <https://doi.org/10.1103/PhysRevLett.96.018001>, 2006.

559 Anderson, R. S., Haff, P. K.: Wind modification and bed response during saltation of sand in air, *Acta*
560 *Mechanica Supplementum*, 1, 21-51, https://doi.org/10.1007/978-3-7091-6706-9_2, 1991.

561 Baas, A. C. W., Sherman, D. J.: Formation and behavior of aeolian streamers, *Journal of Geophysical*
562 *Research: Atmospheres*, 110, F03011, <https://doi.org/10.1029/2004JF000270>, 2005.

563 Baas, A. C. W., Sherman, D. J.: Spatiotemporal variability of aeolian sand transport in a coastal dune
564 environment, *Journal of Coastal Research*, 22, 1198-1205, <https://doi.org/10.2112/06-0002.1>, 2006.

565 Bagnold, R. A.: *The physics of blown sand and desert dunes*, Springer Netherlands,
566 https://doi.org/10.1007/978-94-009-5682-7_17, 1941.

567 Balakumar, B. J., Adrian, R. J.: Large- and very-large-scale motions in channel and boundary-layer flows,
568 *Philos Trans A Math Phys Eng*, 365, 665-681, <https://doi.org/10.1098/rsta.2006.1940>, 2007.

569 Butterfield, G. R.: Transitional behaviour of saltation: wind tunnel observations of unsteady winds,

570 Journal of Arid Environments, 39, 377–394, <https://doi.org/10.1006/jare.1997.0367>, 1998.

571 Carneiro, M. V., Rasmussen, K. R., Herrmann, H. J.: Bursts in discontinuous Aeolian saltation, *Scientific*
572 *Reports*, 5, 1-8, <https://doi.org/10.1038/srep11109>, 2015.

573 Clift, R., Grace, J. R., Weber, M. E.: *Bubbles, drops and particles*, New York: Academic,
574 <https://doi.org/doi:10.1080/07373939308916817>, 1978.

575 Clifton, A., Rüedi, J. D., Lehning, M.: Snow saltation threshold measurements in a drifting-snow wind
576 tunnel, *Journal of Glaciology*, 52, 585-596, <https://doi.org/10.3189/172756506781828430>, 2006.

577 Comola, F., Lehning, M.: Energy- and momentum-conserving model of splash entrainment in sand and
578 snow saltation, *Geophysical Research Letters*, 44, 1601–1609, <https://doi.org/10.1002/2016GL071822>,
579 2017.

580 Creyssels, M., Dupont, P., Ould El Moctar, A., Valance, A., Cantat, I., Jenkins, J. T., Pasini, J. M.,
581 Rasmussen, K. R.: Saltating particles in a turbulent boundary layer: experiment and theory, *Journal of*
582 *Fluid Mechanics*, 625, 47-74, <https://doi.org/10.1017/s0022112008005491>, 2009.

583 Dong, Z., Liu, X., Wang, H., Wang, X.: Aeolian sand transport: a wind tunnel model, *Sedimentary*
584 *Geology*, 161, 71-83, [https://doi.org/10.1016/S0037-0738\(02\)00396-2](https://doi.org/10.1016/S0037-0738(02)00396-2), 2003.

585 Dupont, S., Bergametti, G., Marticorena, B., Simoëns, S.: Modeling saltation intermittency, *Journal of*
586 *Geophysical Research: Atmospheres*, 118, 7109-7128, <https://doi.org/10.1002/jgrd.50528>, 2013.

587 Ellis, J. T., Sherman, D. J., Farrell, E. J., Li, B.: Temporal and spatial variability of aeolian sand transport:
588 Implications for field measurements, *Aeolian Research*, 3, 379-387,
589 <https://doi.org/10.1016/j.aeolia.2011.06.001>, 2012.

590 Feng, S. J., Wang, P.: The influences of boundary layer thickness on the characteristics of saltation sand
591 flow—A large eddy simulation study, *Aeolian Research*, 60, 100853,
592 <https://doi.org/10.1016/j.aeolia.2023.100853>, 2023.

593 Guala, M., Hommema, S. E., Adrian, R. J.: Large-scale and very-large-scale motions in turbulent pipe
594 flow, *Journal of Fluid Mechanics*, 554, 521-542, <https://doi.org/10.1017/S0022112006008871>, 2006.

595 Huang, N., He, P. L., Zhang, J.: Large-eddy simulation of sand transport under unsteady wind,
596 *Geomorphology*, 358, 107105, <https://doi.org/10.1016/j.geomorph.2020.107105>, 2020.

597 Jia, S. M., Wang, Z. S.: Simulation of aerodynamic entrainment with inter-particle cohesions based on
598 discrete element method, *Earth Surface Processes and Landforms*, 46, 1410-1418,
599 <https://doi.org/10.1002/esp.5109>, 2021.

600 Jia, S. M., Wang, Z. S.: A new ejection model for aeolian splash, *Catena*, 213, 106191,
601 <https://doi.org/10.1016/j.catena.2022.106191>, 2022.

602 Jin, T., Chen, Z. Z., Wang, P.: Performance assessment of wall-modeled large-eddy simulation for
603 modeling aeolian two-phase flow, *European Journal of Mechanics / B Fluids*, 100, 291-301,
604 <https://doi.org/10.1016/j.euromechflu.2023.04.008>, 2023.

605 Jin, T., Wang, P., Cao, B.: Transport characteristics of aeolian sand near different thresholds, *Catena*, 247,
606 108541, <https://doi.org/10.1016/j.catena.2024.108541>, 2024.

607 Jin, T., Wang, P., Zheng, X. J.: Characterization of wind-blown sand with near-wall motions and
608 turbulence: from grain-scale distributions to sediment transport, *Journal of Geophysical Research: Earth*
609 *Surface*, 126, <https://doi.org/doi:10.1029/2021JF006234>, 2021.

610 Kawamura, R.: Study on sand movement by wind, *Institute of Science and Technology*, 5, 95-112, 1951.

611 Kim, K., Baek, S. J., Sung, H. J.: An implicit velocity decoupling procedure for the incompressible
612 Navier-Stokes equations, *International Journal for Numerical Methods in Fluids*, 38, 125-138,
613 <https://doi.org/10.1002/flid.205>, 2002.

614 Kok, J. F.: Difference in the wind speeds required for initiation versus continuation of sand transport on
615 mars: Implications for dunes and dust storms, *Physical Review Letters*, 104, 074502,
616 <https://doi.org/10.1103/PhysRevLett.104.074502>, 2010a.

617 Kok, J. F.: An improved parameterization of wind-blown sand flux on Mars that includes the effect of
618 hysteresis, *Geophysical Research Letters*, 37, 986-992, <https://doi.org/10.1029/2010GL043646>, 2010b.

619 Kok, J. F., Renno, N. O.: A comprehensive numerical model of steady state saltation (COMSALT),
620 *Journal of Geophysical Research*, 114, D17204, <https://doi.org/10.1029/2009jd011702>, 2009.

621 Lämmel, M., Dzikowski, K., Kroy, K., Oger, L., Valance, A.: Grain-scale modeling and splash
622 parametrization for aeolian sand transport, *Physical Review E*, 95, 022902,
623 <https://doi.org/10.1103/PhysRevE.95.022902>, 2017.

624 Leenders, J. K., Boxel, J. H., Sterk, G.: Wind forces and related saltation transport, *Geomorphology*, 71,
625 357-372, <https://doi.org/10.1016/j.geomorph.2005.04.008>, 2005.

626 Li, G., Zhang, J., Herrmann, H. J., Shao, Y. P., Huang, N.: Study of aerodynamic grain entrainment in
627 aeolian transport, *Geophysical Research Letters*, 47, <https://doi.org/10.1029/2019GL086574>, 2020a.

628 Li, S. H., Li, C., Yao, D., Ge, X. D., Zhang, G. P.: Wind tunnel experiments for dynamic modeling and
629 analysis of motion trajectories of wind-blown sands, *The European Physical Journal E*, 43, 22,
630 <https://doi.org/10.1140/epje/i2020-11945-0>, 2020b.

631 Liu, H. Y., Feng, Y. E., Zheng, X. J.: Experimental investigation of the effects of particle near-wall
632 motions on turbulence statistics in particle-laden flows, *Journal of Fluid Mechanics*, 943, A8,
633 <https://doi.org/10.1017/jfm.2022.407>, 2022.

634 Liu, H. Y., Shi, Y. X., Zheng, X. J.: Evolution of turbulent kinetic energy during the entire sandstorm
635 process, *Atmos. Chem. Phys.*, 22, 8787-8803, <https://doi.org/10.5194/acp-2021-889>, 2021.

636 Lu, H., Raupach, M. R., Richards, K. S.: Modeling entrainment of sedimentary particles by wind and
637 water: A generalized approach, *Journal of Geophysical Research: Atmospheres*, 110,
638 <https://doi.org/10.1029/2005JD006418>, 2005.

639 Martin, R. L., Kok, J. F.: Distinct thresholds for the initiation and cessation of aeolian saltation from field
640 measurements, *Journal of Geophysical Research: Earth Surface*, 123, 1546-1565,
641 <https://doi.org/10.1029/2017jf004416>, 2018.

642 Marusic, I., Baars, W. J., Hutchins, N.: Scaling of the streamwise turbulence intensity in the context of
643 inner-outer interactions in wall turbulence, *Physical Review Fluids*, 2, 100502,
644 <https://doi.org/10.1103/PhysRevFluids.2.100502>, 2017.

645 Marusic, I., Mckeon, B. J., Monkewitz, P. A., Nagib, H. M., Smits, A. J., Sreenivasan, K. R.: Wall-
646 bounded turbulent flows at high Reynolds numbers: Recent advances and key issues, *Physics of Fluids*,
647 22, 065103, <https://doi.org/10.1063/1.3453711>, 2010.

648 Mathis, R., Hutchins, N., Marusic, I.: Large-scale amplitude modulation of the small-scale structures in
649 turbulent boundary layers, *Journal of Fluid Mechanics*, 628, 311-337,
650 <https://doi.org/10.1017/S0022112009006946>, 2009.

651 Pähtz, T., Clark, A. H., Valyrakis, M., Durán, O.: The Physics of sediment transport initiation, cessation,
652 and entrainment across aeolian and fluvial environments, *Reviews of Geophysics*, 58, e2019RG000679,
653 <https://doi.org/10.1029/2019RG000679>, 2020.

654 Pähtz, T., Valyrakis, M., Zhao, X. H., Li, Z. S.: The critical role of the boundary layer thickness for the
655 initiation of aeolian sediment transport, *Geosciences*, 8, 314,
656 <https://doi.org/10.3390/geosciences8090314>, 2018.

657 Parajuli, S. P., Zobeck, T. M., Kocurek, G., Yang, Z. L., Stenchikov, G. L.: New insights into the wind-

658 dust relationship in sandblasting and direct aerodynamic entrainment from wind tunnel experiments,
659 *Journal of Geophysical Research: Atmospheres*, 121, 1776-1792, <https://doi.org/10.1002/2015JD024424>,
660 2016.

661 Porté-Agel, F., Meneveau, C., Parlange, M. B.: A scale-dependent dynamic model for large-eddy
662 simulation: application to a neutral atmospheric boundary layer, *Journal of Fluid Mechanics*, 415, 261-
663 284, <https://doi.org/10.1017/S0022112000008776>, 2000.

664 Rasmussen, K. R., Sørensen, M.: Aeolian mass transport near the saltation threshold, *Earth Surface
665 Processes and Landforms*, 24, 413-422, [https://doi.org/10.1002/\(SICI\)1096-
666 9837\(199905\)24:5<413::AID-ESP997>3.0.CO;2-I](https://doi.org/10.1002/(SICI)1096-9837(199905)24:5<413::AID-ESP997>3.0.CO;2-I), 1999.

667 Schlatter, P., Örlü, R.: Assessment of direct numerical simulation data of turbulent boundary layers,
668 *Journal of Fluid Mechanics*, 659, 116-126, <https://doi.org/10.1017/S0022112010003113>, 2010.

669 Serafimovich, A., Thomas, C., Foken, T.: Vertical and horizontal transport of energy and matter by
670 coherent motions in a tall spruce canopy, *Boundary-Layer Meteorology*, 140, 429-451,
671 <https://doi.org/10.1007/s10546-011-9619-z>, 2011.

672 Shao, Y. P.: *Physics and modelling of wind erosion*, Heidelberg: Springer, 2008.

673 Shao, Y. P., Li, A.: Numerical modelling of saltation in the atmospheric surface layer, *Boundary-Layer
674 Meteorology*, 91, 199-225, <https://doi.org/10.1023/A:1001816013475>, 1999.

675 Sherman, D. J., Houser, C., Ellis, J. T., Farrell, E. J., Li, B. L., Davidson-Arnott, R. G. D., Baas, A. C.
676 W., Maia, L. P.: Characterization of aeolian streamers using time-average videography, *Journal of Coastal
677 Research*, 165, 1331-1336, <https://doi.org/10.2112/si65-225.1>, 2013.

678 Sherman, D. J., Jackson, D., Namikas, S. L., Wang, J.: Wind-blown sand on beaches: an evaluation of
679 models, *Geomorphology*, 22, 113-133, [https://doi.org/10.1016/s0169-555x\(97\)00062-7](https://doi.org/10.1016/s0169-555x(97)00062-7), 1998.

680 Smits, A. J., McKeon, B. J., Marusic, I.: High-Reynolds number wall turbulence, *Annual Review of
681 Fluid Mechanics*, 43, 353-375, <https://doi.org/10.1146/annurev-fluid-122109-160753>, 2011.

682 Spies, P. J., Mcewan, I. K., Butterfield, G. R.: One-dimensional transitional behaviour in saltation, *Earth
683 Surface Processes and Landforms*, 25, 505-518, [https://doi.org/10.1002/\(SICI\)1096-
684 9837\(200005\)25:5<505::AID-ESP78>3.0.CO;2-D](https://doi.org/10.1002/(SICI)1096-9837(200005)25:5<505::AID-ESP78>3.0.CO;2-D), 2000.

685 Stout, J. E., Zobeck, T. M.: Intermittent saltation, *Sedimentology*, 44, 959-970,
686 <https://doi.org/10.1046/j.1365-3091.1997.d01-55.x>, 1997.

687 Tholen, K., Pähtz, T., Kamath, S., Parteli, E. J. R., Kroy, K.: Anomalous scaling of aeolian sand transport
688 reveals coupling to bed rheology, *Physical Review Letters*, 130, 058204,
689 <https://doi.org/10.1103/PhysRevLett.130.058204>, 2023.

690 Wang, P., Feng, S. J., Zheng, X. J., Sung, H. J.: The scale characteristics and formation mechanism of
691 aeolian sand streamers based on large eddy simulation, *Journal of Geophysical Research: Atmospheres*,
692 124, 11372-11388, <https://doi.org/10.1029/2019JD031081>, 2019.

693 Wang, P., Zheng, X. J.: Saltation transport rate in unsteady wind variations, *European Physical Journal
694 E*, 37, 1-11, <https://doi.org/10.1140/epje/i2014-14040-3>, 2014.

695 Wang, Z. T., Zhang, C. L., Wang, H. T.: Intermittency of aeolian saltation, *European Physical Journal E*,
696 37, 1-6, <https://doi.org/10.1140/epje/i2014-14126-x>, 2014.

697 White, B. R.: Soil transport by winds on mars, *Journal of Geophysical Research*, 84, 4643-4651,
698 <https://doi.org/10.1029/JB084iB09p04643>, 1979.

699 Williams, J. J., Butterfield, G. R., Clark, D. G.: Rates of aerodynamic entrainment in a developing
700 boundary layer, *Sedimentology*, 37, 1039-1048, <https://doi.org/10.1111/j.1365-3091.1990.tb01844.x>,
701 1990.

702 Williams, J. J., Butterfield, G. R., Clark, D. G.: Aerodynamic entrainment threshold: effects of boundary
703 layer flow conditions, *Sedimentology*, 41, 309-328, <https://doi.org/10.1111/j.1365-3091.1994.tb01408.x>,
704 1994.

705 Yang, X., Sadique, J., Mittal, R., Meneveau, C.: Integral wall model for large eddy simulations of wall-
706 bounded turbulent flows, *Physics of Fluids*, 27, 025112, <https://doi.org/10.1063/1.4908072>, 2015.

707 Zhang, J., Li, G., Shi, L., Huang, N., Shao, Y. P.: Impact of turbulence on aeolian particle entrainment:
708 results from wind-tunnel experiments, *Atmos. Chem. Phys.*, 22, 9525-9535, [https://doi.org/10.5194/acp-](https://doi.org/10.5194/acp-22-9525-2022)
709 22-9525-2022, 2022.

710 Zheng, X. J., Jin, T., Wang, P.: The influence of surface stress fluctuation on saltation sand transport
711 around threshold, *Journal of Geophysical Research: Earth Surface*, 125, e2019JF005246,
712 <https://doi.org/10.1029/2019jf005246>, 2020.

713 Zhou, Y. H., Guo, X., Zheng, X. J.: Experimental measurement of wind-sand flux and sand transport for
714 naturally mixed sands, *Physical Review E*, 66, 021305, <https://doi.org/10.1103/PhysRevE.66.021305>,
715 2002.

716 Zhu, H. Y., Pan, C., Wang, J. J., Liang, Y. R., Ji, X. C.: Sand-turbulence interaction in a high-reynolds-
717 number turbulent boundary layer under net sedimentation conditions, *International Journal of Multiphase*
718 *Flow*, 119, 56-71, <https://doi.org/10.1016/j.ijmultiphaseflow.2019.07.001>, 2019.